Comparison of Microinstability Properties for Stellarator Magnetic Geometries

G. Rewoldt,* L.-P. Ku, and W.M. Tang

Princeton Plasma Physics Laboratory,

Princeton University, Princeton, New Jersey 08543-0451

Abstract

The microinstability properties of seven distinct magnetic geometries corresponding to different operating and planned stellarators with differing symmetry properties are compared. Specifically, the kinetic stability properties (linear growth rates and real frequencies) of toroidal microinstabilities (driven by ion temperature gradients and trapped-electron dynamics) are compared, as parameters are varied. The familiar ballooning representation is used to enable efficient treatment of the spatial variations along the equilibrium magnetic field lines. These studies provide useful insights for understanding the differences in the relative strengths of the instabilities caused by the differing localizations of good and bad magnetic curvature and of the presence of trapped particles. The associated differences in growth rates due to magnetic geometry are large for small values of the temperature gradient parameter $\eta \equiv d\ln T/d\ln n$, whereas for large values of η, the mode is strongly unstable for all of the different magnetic geometries.

PACS numbers: 52.35.Qz,52.65.Tt,52.55.Hc

I. INTRODUCTION

The differing magnetic geometries of different stellarator designs have implications for microinstabiities. More specifically, the different regions of localization, along a chosen magnetic field line, of "good" (stabilizing) and "bad" (destabilizing) magnetic curvature and of trapped particles can affect the linear growth rates of microinstabilities such as the ion-temperature-gradient-trapped-electron modes (ITG-TEM modes). Here, we will compare linear growth rates and real frequencies for these modes using the non-axisymmetric or stellarator version[1] of the FULL microinstability code,[2,3] which employs the ballooning representation,[4] so that the corresponding lowest-order eigenfrequency-eigenfunction calculation, along a chosen magnetic field line, is radially local. We will consider seven different cases corresponding to different operating and planned stellarator devices of different intrinsic symmetry properties. The first case is for the Large Helical Device[5] (LHD), which is not quasi-symmetric. The second case is for the National Compact Stellarator Experiment[6] (NCSX), which is a quasi-axisymmetric design. This case has a non-zero net current. The third case is a variant NCSX case with zero net current (NCSX-J=0). The fourth case corresponds to the Wendelstein 7-X (W7-X) design,[7] which was designed using a confinement principle later called quasi-isodynamicity.[8] The fifth case is for the Helically Symmetric Experiment[9] (HSX), which is quasi-helically symmetric. The sixth case is for the Quasi-Poloidal Stellarator[10] (QPS). In order to make some contact with corresponding tokamak results, the seventh case (NCSX-SYM) is axisymmetric, obtained from the NCSX case by arbitrarily setting all of the (toroidal mode number) $n \neq 0$ Fourier coefficients for the magnetic field to zero in the input to the magnetohydrodynamic (MHD) equilibrium calculation. For all of these cases, the geometric-center major radius, and the magnetic field strength at this major radius, are normalized to be the same. Also, the pressure profile used in the MHD equilibrium calculations is the same for all of the cases (and correspondingly the density and temperature profiles used for the FULL code microinstability calculations), and are based on those published in Fig. 4 of Ref. 11 for a particular (inward-shifted) LHD experimental discharge, so that they will be in some sense experimentally-realizable. Also, all of the cases are normalized here to the same, very low, volume-average β (= plasma pressure / magnetic pressure) value. Thus, the differences in the microinstability results that we obtain come purely from the different magnetic field Fourier coefficients used as input for the MHD

equilibrium calculations for the seven cases.

The FULL code has previously been applied, for studies of stellarator microinstabilities, to an earlier design for NCSX in Ref. 1, and to several LHD experimentally-derived cases in Refs. 12 and 13, in the radially-local limit using the ballooning representation, and including trapped-electron effects. Other kinetic calculations of ITG modes in stellarator geometry have been done in Refs. 14 and 15, using the radially-global EUTERPE code,[16,17] for cases based on HSX and W7-X, but only in the limit of adiabatic electron response. The calculation of Ref. 15 has recently been extended for finite-β MHD equilibria for W7-X in Ref. 18. Other calculations using more approximate kinetic mode equations have been carried out for W7-X and LHD in Refs. 19 and 20. The present work is the first to include realistic trapped-electron effects, for comparison of these different stellarator magnetic geometries, in order to investigate the effects of the differing trapped-electron localization and bad curvature localization on the linear growth rates.

The input for the numerical MHD equilibrium calculation, and the equilibrium calculation itself, are further described in Sec. II. The FULL code microinstability calculation and the particular instability considered are described in Sec. III. The results for the effects of the variation of the parameters on the linear growth rate and the real frequency are presented in Sec. IV. Conclusions are presented in Sec. V.

II. MHD EQUILIBRIA

This section presents plasma equilibrium characteristics at (volume-average) $\beta = 0.1\%$ for the LHD, NCSX, NCSX-J=0, W7-X, HSX, and QPS cases, as well as the NCSX-SYM "tokamak" case. These equilibria were constructed based on VMEC MHD equilibrium calculations[21,22] for fixed plasma boundaries with the last closed magnetic surface defined by (1) for LHD, the inward-shifted plasma for experimental shot 11369 at $t = 2.2$ s; (2) for NCSX, the so-called M50 coils at 4% β, and (3) for NCSX-J=0, a high iota, vacuum start-up configuration; (4) for W7-X, the standard high mirror ratio configuration; (5) for HSX, the reconstructed plasma for standard operations; (6) for QPS, the reference two field-period vacuum configuration, and (7) for the "tokamak" NCSX-SYM, the axially symmetric components of NCSX. In all cases the major radius was normalized to 3.6 m and the magnetic field on axis to 1.5 T. In the VMEC calculations, 61 radial grids, 11 poloidal modes and

13 toroidal modes were used, except for the HSX case, for which 31 toroidal modes were used instead, because of the large number of modes used in fitting the plasma boundary. The pressure profile used is derived from the measured electron temperature and density profiles of an LHD experimental discharge. Except for NCSX, the net current is assumed to be zero. For NCSX, the current density expected from the bootstrap current at 4% β was used. This current density was based on a broader pressure profile; thus it may not be fully consistent with that based on the experimental profiles from LHD used in the present set of calculations.

In Fig. 1, we show the plain view of the last closed magnetic surface (LCMS), along with the contours of magnetic field strength on that surface (red = strongest, blue = weakest) for the different cases. A plot for the NCSX-J=0 case is not shown because of its similarity to the NCSX result. The subfigures show the typical characteristics expected of each device. In particular, it is quite evident that in NCSX the magnetic spectrum is dominated by the toroidal terms, in LHD by the $m = 2$, $n = 1$ component, in W7-X and QPS by the mirror term $m = 0$, $n = 1$ (with mirror ratios 10% and 18%, respectively), and in HSX, by the helical term $m = 1$, $n = 1$. (Here, m is the poloidal mode number and n is the toroidal mode number.)

Fig. 2 shows the rotational transform profiles as a function of the normalized toroidal flux s ($s \propto r^2$). The rotation of the ellipse and the large number of field periods in the LHD case give rise to high shear in the rotational transform profile. On the other hand, the shear in the NCSX case is almost entirely due to the plasma current. Typically, finite plasma pressure reduces the transform at the edge. In the W7-X case, the edge rotational transform will be less than one at 5% β, and the $m = 5$ resonance is avoided at the operating pressure. The number of toroidal periods M and the calculated aspect ratio based on the plasma volume are given in Table I for each case.

The three-dimensional MHD equilibium code VMEC works in VMEC coordinates. The resulting MHD equilibria are transformed into Boozer coordinates[23] by the TERPSICHORE code,[24] with the numbers of Fourier harmonics retained in the Boozer coordinates being about twice the numbers used in the VMEC equilibrium calculations. The quantities needed for the FULL code calculation along a single chosen magnetic field line are constructed by the VVBAL code.[25] For all of the cases here, we choose the magnetic surface with $s = 0.74$, which is at or close to that which maximizes the linear growth rate for the LHD case. The

particular magnetic field line chosen on this magnetic surface is specified by $\alpha \equiv \zeta - q\theta$; α will be varied for each case to maximize the linear growth rate. In addition, in the ballooning representation, the "ballooning parameter" θ_0 (also called θ_k) must be chosen; θ_0 will also be varied for each case to maximize the linear growth rate.

III. MICROINSTABILITY CALCULATION

The FULL code solves the linearized gyrokinetic equation and the quasineutrality condition. It includes trapped particle effects, finite Larmor radius effects to all orders (complete Bessel functions), and bounce frequency and transit frequency and magnetic drift frequency resonances, for all included plasma species. The FULL code automatically finds all of the trapped particle classes for any pitch angle, for the input variation of the magnetic field strength along the chosen magnetic field line. The calculation is in the collisionless, electrostatic limit. In this limit, it has been compared[26] for a stellarator case with the GS2 initial value code,[27] showing good agreement. The FULL code was previously applied[13] for the present LHD case in a more experimentally realistic manner, including two impurity species and a hot beam species. In the present work, since the emphasis is on the differences caused by the different magnetic geometries in the microinstability growth rates and real frequencies, we include only electron (e) and thermal hydrogen (i) species, with $n_i = n_e$ and $T_i = T_e$ on all surfaces.

In the collisionless, electrostatic limit, for $k_\theta \rho_i \lesssim 1$, the instabilities of interest are the ion temperature gradient (ITG) mode and the (collisionless) trapped electron mode (TEM mode). For the present cases, these modes "hybridize" to form a single unstable root, which we call the ITG-TEM root. For small values of $\eta_i \equiv (d \ln T_i)/(d \ln n_e)$, this root is destabilized only by the collisionless trapped electron mode (CTEM) destabilization mechanism, and has a real frequency in the electron diamagnetic direction. The CTEM mechanism is a resonance mechanism coming from the trapped-electron orbit-time-average term, involving resonance between the mode frequency ω and the orbit-time-average electron magnetic drift frequency, $\omega_{de}^{(0)}$. The value of $\omega_{de}^{(0)}$ for any given pitch angle depends on the trapped electron orbit extent along the magnetic field line, and on the distribution of good and bad magnetic curvature along the magnetic field line. The effects of these, for a specific root, is weighted by the linear eigenfunction along the magnetic field line for that root. For large values of η_i,

the root is destabilized both by the CTEM mechanism and by the ITG mechanism, and has a real frequency in the ion diamagnetic direction. The ITG mechanism is a non-resonant mechanism which operates only above a critical value η_i^c (which is typically of order 1.0 to 1.5) of η_i, and is only moderately affected by the ion magnetic drift frequency; the ITG mechanism is stronger at shorter effective connection lengths along the magnetic field line. At an intermediate value of η_i, the real frequency of this hybrid root makes a transition from the electron diamagnetic direction to the ion diamagnetic direction.

The input functions $|B(\theta)|$, versus the ballooning (non-periodic) poloidal angle coordinate θ along the magnetic field line, from $-\pi$ to π, are shown for the seven cases in Fig. 3. Illustrative trapped-particle orbit extents in θ are shown by the thick lines for one or more illustrative pitch angles for each case. These profiles are evaluated for the values α^{Max} of α, and θ_0^{Max} of θ_0, which maximize the linear growth rate of the hybrid root for each case. The numerical values of α^{Max} and θ_0^{Max} for the seven cases are given in Table I. The results for the maximization process are given in Sec. IV. The corresponding input functions $k_\perp^2(\theta)/n^2$ (*i.e.*, $k_\perp^2(\theta) \propto n^2$ for $n = 1$) for the seven cases for these same values of α and θ_0 are shown in Fig. 4. The corresponding input functions for the magnetic curvature function $\mathbf{k}_\perp \cdot \{\mathbf{b} \times [(\mathbf{b} \cdot \nabla)\mathbf{b}]\}(\theta)/n$ (*i.e.*, $\mathbf{k}_\perp \cdot \{\mathbf{b} \times [(\mathbf{b} \cdot \nabla)\mathbf{b}]\}(\theta) \propto n$ for $n = 1$) for the seven cases for these same values of α and θ_0 are shown in Fig. 5. In Fig. 5, bad (destabilizing) curvature is positive and good (stabilizing) curvature is negative. Note that the symmetry in θ for the functions in Figs. 3, 4, and 5 is slightly broken for the W7-X, HSX, and QPS cases by their nonzero values of α^{Max}.

IV. RESULTS

In this section we will maximize the linear growth rate for the hybrid root successively over α, θ_0, and $k_\theta(\theta = 0)\rho_i \propto n$ (this order is somewhat arbitrary), for each of the seven cases. The resulting values give roughly a simultaneous maximum of the growth rates in these three parameters; the maximization could be slightly further improved by additional scans over the three parameters, but that would be excessively computationally expensive. Then we will vary $\eta = \eta_i = \eta_e$ from the LHD experimental value; this η variation will give us information about the strengths of the two destabilization mechanisms for this root, as they differ among the seven cases.

We start by varying α for each case, taking $\theta_0 = 0$, $k_\theta(\theta = 0)\rho_i = 0.30$, and $\eta_i = \eta_e = 2.66$, the LHD experimental value. We vary $M\alpha$ from 0 to π; since each of the equilibria is symmetric around both $M\alpha = 0$ (the start of a period) and $M\alpha = \pi$ (the half-period value), this covers the entire range of variation of the growth rate and real frequency. The results of this variation for the linear growth rate γ and real frequency ω_r for the seven cases are shown in Fig. 6. The values α^{Max} of α that maximize the growth rates are given in Table I. Four of them are zero and the other three are non-zero. Of course, since the choice of origin in α is arbitrary, there is no requirement that the extremal value of α be zero in general. For our axisymmetric NCSX-SYM case, the result is independent of α, and we arbitrarily use $\alpha = 0$ for the remaining calculations.

Then, taking $\alpha = \alpha^{Max}$ for each case, and again with $k_\theta(\theta = 0)\rho_i = 0.30$ and $\eta_i = \eta_e = 2.66$, we vary θ_0 from 0 to π; again because of the symmetry and periodicity in θ_0, this covers the entire range of variation in θ_0. The results of this variation of θ_0 for the seven cases are shown in Fig. 7. For all seven cases, we find that $\theta_0^{Max} = 0$. This is also the most common result in tokamak cases, since the choice $\theta_0 = 0$ allows the eigenfunction to localize around $\theta = 0$, where the bad curvature and the trapped electron fraction are both a maximum, thereby maximizing the growth rate. Similar considerations apply here for the stellarator cases, though the variation in θ of the magnetic field strength in Fig. 3 and of the magnetic curvature in Fig. 5 are more complicated.

Next, we vary $k_\theta(\theta = 0)\rho_i \propto n$, from zero to one, for $\alpha = \alpha^{Max}$ and $\theta_0 = \theta_0^{Max} = 0$ and $\eta = \eta_i = \eta_e = 2.66$ for each case. The results of this variation are shown in Fig. 8. The values $k_\theta^{Max}(\theta = 0)\rho_i$ of $k_\theta(\theta = 0)\rho_i$ that maximize the growth rates are given in Table I. They vary from 0.25 to 0.775. However, the exceptional case is the W7-X case, where the growth rate plateaus for $k_\theta(\theta = 0)\rho_i$ above one, instead of having a local maximum (several other cases almost plateau in the same way). For the W7-X case, therefore, we arbitrarily choose to use $k_\theta(\theta = 0)\rho_i = 1.0$ for the remaining calculations.

The linear eigenfunctions in the (nonperiodic) ballooning angle θ for the hybrid root, for these maximizing values of α, θ_0, and $k_\theta(\theta = 0)\rho_i$, are shown for the seven cases in Fig. 9. Note that the (complex) normalization is arbitrary for these eigenfunctions. All of them have (half) width (at half maximum) from of order one radian or less, up to about two radians.

Finally, we vary $\eta = \eta_i = \eta_e$ from zero to four for each of these cases, for the maximizing

values of α, θ_0, and $k_\theta(\theta = 0)\rho_i$. This variation will give us additional information about the CTEM and ITG destabilization mechanisms for each of these cases. In this process, the total pressure gradient is kept constant, so as to maintain consistency with the MHD equilibrium. This means, for instance, that as η_i and η_e increase, and thus as the ion temperature gradient and the electron temperature gradient increase, the electron and ion density gradient decreases. The results of this variation are shown in Fig. 10. As mentioned, the real frequency makes a transition from the electron diamagnetic direction to the ion diamagnetic direction as η increases. All of the seven cases are strongly unstable for η values at the upper end of the η range, where both the ITG and CTEM mechanisms are operative. All of the cases have roughly comparable linear growth rates there, except for the HSX case, which has a substantially higher growth rate. This is due to the facts that the HSX case has both a short effective connection length (which enhances the ITG mechanism) and substantial bad curvature at $\theta = 0$ (which enhances the CTEM mechanism), and is the only case with both of these attributes. Then, as η is reduced from this range to be below η_i^c, the ITG mechanism turns off, leaving only the CTEM mechanism operative. What happens for each of the cases for small η depends on the details of the bad curvature localization and the trapped particle localization, as weighted by the eigenfunction. For this kind of η-variation where the density gradient increases as the temperature gradients decrease, for a nearly circular cross-section tokamak the growth rate can have a strong increase, below a minimum for $\eta \simeq \eta_i^c$, with a maximum at $\eta = 0$, as seen in Fig. 4 of Ref. 28. On the other hand, for a strongly non-circular cross-section tokamak, where the bad curvature is much weaker near $\theta = 0$, the rise in growth rate can be much weaker, with the maximum growth rate away from $\eta = 0$, as seen in Fig. 1 of Ref. 28. In the present stellarator cases, a range of behaviours is seen, from the NCSX-J=0, NCSX, and LHD cases, which have local maxima in the growth rate at $\eta = 0$, to the HSX, W7-X, and NCSX-SYM cases, whose growth rates decrease monotonically down to $\eta = 0$ (though the overall destabilization of the HSX case is much larger), to the QPS case, which is completely stable for $\eta \lesssim 0.5$. The implications of these different types of variation will be discussed in Sec. V.

It is worthwhile examining the most extreme case, the QPS case, to see in more detail how this stabilization comes about for small η, when only the CTEM mechanism is operative. From Fig. 9, the half-width at half-maximum of the eigenfunction for the QPS case is about 0.4 radians (this figure is for $\eta = 2.66$, but the eigenfunction has about the same width for

$\eta = 0.5$), so that anything much outside $|\theta| = 0.4$ radians will have a weak influence on the growth rate. In the magnetic field strength variation for the QPS case in Fig. 3, the most deeply trapped particles are localized in two wells centered around $\theta = -0.4$ radians and around $\theta = 0.4$ radians. However, the curvature is almost zero for the QPS case near $\theta = -0.4$ radians and near $\theta = 0.4$ radians. The next most deeply trapped particles are centered around $\theta = 0$, but with turning points near -0.6 radians and 0.4 radians. Deeply trapped particles spend most of the time in their orbits near their turning points, so this class of trapped particles will also strongly weight the near-zero curvature regions near $\theta = -0.4$ radians and near $\theta = 0.4$ radians. The other classes of trapped particles will spend most of the time in their orbits away from the region most strongly weighted by the eigenfunction. The total destabilization will thus be weak, and unable to overcome the damping due to ion transit frequency resonances (ion Landau damping) for untrapped ions, bounce frequency resonances for trapped ions, magnetic drift frequency resonances, *etc.* The net result of all of these contributions can only be evaluated numerically, and that is what is done in the FULL code calculation for the QPS case and for the other cases.

V. CONCLUSIONS

We have compared the microinstability properties of a number of different stellarator magnetic geometries for particular configurations for the LHD, NCSX, W7-X, HSX, and QPS stellarators. For NCSX, we have examined the present NCSX design with non-zero net current, and a variant, NCSX-J=0, with zero net current, but there is little difference between them for the microinstability results. We have also examined an axisymmetric version of the NCSX MHD equilibrium, NCSX-SYM. All of these cases have MHD equilibrium input normalized to the same geometric-center major radius, and to the same magnetic field strength at that major radius, and all use the same pressure profile as a function of the normalized toroidal flux, (derived from published LHD electron density and temperature profiles), all at the same very low volumn-average β value. The results might differ somewhat for other choices of the pressure profile, or for another choice of the single magnetic surface on which the instability calculation is performed. The linear growth rate and the real frequency are calculated by the nonaxisymmetric version of the FULL code, in the collisionless, electrostatic limit, for a particular hybrid root, which contains the usual ITG and

TEM modes. The growth rates on the chosen magnetic surface are maximized over the field line label $\alpha \equiv \zeta - q\theta$, over the ballooning parameter θ_0 (or θ_k), and over $k_\theta(\theta = 0)\rho_i \propto n$, for each case, for the LHD experimental value of $\eta = \eta_i = \eta_e = 2.66$. For these maximizing values of α, θ_0, and $k_\theta(\theta = 0)\rho_i$, η is then varied from high values where both the ITG and the CTEM destabilization mechanisms contribute, down to low values where only the CTEM mechanism contributes. The CTEM contribution for the different cases depends on the relative localization of trapped particles and of bad magnetic curvature in the region where the linear eigenfunction is large. The seven cases fall into distinct categories: For the NCSX, NCSX-J=0, and LHD cases, the growth rate rises as η approaches zero, indicating a rather strong destabilizing contribution from the CTEM mechanism. For the W7-X, and NCSX-SYM cases, the growth rate is falling as η approaches zero, indicating a weak destabilizing contribution from the CTEM mechanism. (The growth rate for the HSX case is also falling as η approaches zero, but the overall destabization is larger, due to the reasons mentioned in Sec. IV.) The QPS case falls into this same category, but the effect is even stronger, and the mode is completely stabilized for $\eta \lesssim 0.5$.

However, a point that should be emphasized here is that all of these cases are strongly unstable if η is large enough, that is, if the ion temperature gradient is large enough, regardless of the magnetic geometry! Thus, all of these configurations can be expected to be subject to ITG-type instabilities in radial regions of strong ion temperature gradient, even if the trapped-electron destabilization mechanism is weak for a particular magnetic field configuration! The present results are only a first attempt at this kind of comparison, for a single set of density and temperature (and thus pressure) profiles, and will vary quantitatively for other sets of profiles, but this general conclusion should be of wider applicability. However, the effects of sheared rotation, which may be substantial with the various types of quasi-symmetry, are not considered here, and may have the capability of changing these conclusions qualitatively, and thus are also worth further investigation.

Acknowledgments

The authors would like to thank Dr. H. Yamada and Dr. N. Nakajima for providing the LHD case, Prof. J. Nuehrenberg and Dr. V. Kornilov for providing the W7-X case, Mr. W. Guttenfelder and Dr. J. N. Talmadge for providing the HSX case, and Dr. D.

Spong for providing the QPS case. This work was supported by U.S. DOE Contract No. DE-AC02-76-CHO-3073.

---

* rewoldt@pppl.gov

[1] G. Rewoldt, L.-P. Ku, W. M. Tang, and W. A. Cooper, Phys. Plasmas **6**, 4705 (1999).

[2] G. Rewoldt, W. M. Tang, and M. S. Chance, Phys. Fluids **25**, 480 (1982).

[3] G. Rewoldt, W. M. Tang, and R. J. Hastie, Phys. Fluids **30**, 807 (1987).

[4] E. A. Frieman, G. Rewoldt, W. M. Tang, and A. H. Glasser, Phys. Fluids **23**, 1750 (1980); W. Anthony Cooper, Plasma Phys. Controlled Fusion **34**, 1011 (1992).

[5] A. Iiyoshi, A. Komori, A. Ejiri, *et al.*, Nucl. Fusion **39**, 1245 (1999).

[6] G. H. Neilson, M. C. Zarnstorff, L. P. Ku, *et al.,* Proc. 19th Int. Conf. on Fusion Energy (Lyon, 2002) (Vienna: IAEA) CD-ROM file (IC-1) http://www.iaea.org/programmes/ripc/physics/fec2002/html/fec2002.htm

[7] G. Grieger, C. D. Beidler, H. Maasberg, *et al.*, in *Plasma Physics and Controlled Nuclear Fusion Research 1990* (International Atomic Energy Agency, Vienna, 1991), Vol. 3, p. 525.

[8] J. Nührenberg, Europhys. News **6**, 216 (1998).

[9] F. S. B. Anderson, A. F. Almagri, D. T. Anderson, P. G. Matthews, J. N. Talmadge, and J. L. Shohet, Fusion Technol. **27**, 273 (1995).

[10] J. F. Lyon, S. P. Hirshman, D. A. Spong, *et al.*, "Overview of the QPS Project," *Proc. 30th Conf. Controlled Fusion and Plasma Physics*, St. Petersburg, Russia, July 7–11, 2003, European Physical Society (2003), http://epsppd.epfl.ch/StPetersburg/start.html.

[11] H. Yamada, K. Y. Watanabe, K. Yamazaki, *et al.,* Nucl. Fusion **41**, 901 (2001).

[12] G. Rewoldt, L.-P. Ku, W. M. Tang, H. Sugama, N. Nakajima, K. Y. Watanabe, S. Murakami, H. Yamada, and W. A. Cooper, Phys. Plasmas **7**, 4942 (2000).

[13] G. Rewoldt, L.-P. Ku, W. M. Tang, H. Sugama, N. Nakajima, K. Y. Watanabe, S. Murakami, H. Yamada, and W. A. Cooper, Nucl. Fusion **42**, 1047 (2002).

[14] G. Jost, T. M. Tran, W. A. Cooper, L. Villard, and K. Appert, Phys. Plasmas **8**, 3321 (2001).

[15] V. Kornilov, R. Kleiber, R. Hatzky, L. Villard, and G. Jost, Phys. Plasmas **11**, 3196 (2004).

[16] G. Jost, T. M. Tran, K. Appert, W. A. Cooper, and L. Villard, in *Theory of Fusion Plasmas, International Workshop, Varenna, September 1998* (Editrice Compositori, Società Italiana di

Fisica, Bologna, 1999), p. 419.

[17] G. Jost, T. M. Tran, L. Villard, W. A. Cooper, and K. Appert, in *Proceedings of the 26th EPS Conference on Controlled Fusion and Plasma Physics, Maastricht, 1999,* edited by B. Schweer, G. Van Oost, and E. Vietzke (European Physical Society, Maastricht, 1999), p. 1093.

[18] V. Kornilov, R. Kleiber, and R. Hatzky, Nucl. Fusion **45**, 238 (2005).

[19] A. Kendl and H. Wobig, Phys. Plasmas **6**, 4714 (1999).

[20] T. Kuroda, H. Sugama, R. Kanno, and M. Okamoto, J. Phys. Soc. Jpn. **69**, 2485 (2000).

[21] S. P. Hirshman, D. K. Lee, Comput. Phys. Commun. **39**, 161 (1986).

[22] S. P. Hirshman, U. Schwenn, J. Nuehrenberg, J. Comput. Phys. **87**, 396 (1990).

[23] A. H. Boozer, Phys. Fluids **24**, 904 (1980).

[24] D. V. Anderson, W. A. Cooper, R. Gruber, S. Merazzi, U. Schwenn, Int. J. Supercomp. Appl. **4**, 34 (1990).

[25] W. A. Cooper, Plasma Phys. and Controlled Fusion **34**, 1011 (1992).

[26] E. A. Belli, W. Dorland, G. W. Hammett, and M. C. Zarnstorff, Bull. Am. Phys. Soc. **46**, No. 8, 232 (2001).

[27] M. Kotschenreuther, G. Rewoldt, and W. M. Tang, Comp. Phys. Comm. **88**, 128 (1995).

[28] G. Rewoldt and W. M. Tang, Phys. Fluids B **2**, 318 (1990).

FIGURE CAPTIONS

FIG. 1: Variation of magnetic field strength (blue = weakest, red = strongest) on last closed flux surface for LHD, NCSX, W7-X, HSX, QPS, and NCSX-SYM cases.

FIG. 2: Variation of rotational transform $\iota = 1/q$ with magnetic surface label s.

FIG. 3: Variation of magnetic field strength versus non-periodic ballooning coordinate θ on chosen magnetic field line, showing illustrative trapped particle orbit extents.

FIG. 4: Variation of $k_\perp^2/n^2$ versus θ on chosen magnetic field line.

FIG. 5: Variation of magnetic curvature function $\mathbf{k}_\perp \cdot \{\mathbf{b} \times [(\mathbf{b} \cdot \nabla)\mathbf{b}]\}(\theta)/n$ versus θ on chosen magnetic field line.

FIG. 6: Variation of linear growth rate γ and real frequency ω_r versus magnetic field line label $M\alpha \equiv M(\zeta - q\theta)$ on chosen magnetic surface.

FIG. 7: Variation of linear growth rate γ and real frequency ω_r versus ballooning coordinate θ_0 $(= \theta_k)$ on chosen magnetic field line.

FIG. 8: Variation of linear growth rate γ and real frequency ω_r versus $k_\theta(\theta = 0)\rho_i \propto n$.

FIG. 9: Linear eigenfunctions versus non-periodic ballooning coordinate θ, for values of α, θ_0, and $k_\perp(\theta = 0)\rho_i$ that maximize linear growth rate (or $k_\perp(\theta = 0)\rho_i = 1.0$ for W7-X case).

FIG. 10: Variation of linear growth rate γ and real frequency ω_r versus $\eta = \eta_i = \eta_e$.

TABLE I: Parameters for the seven stellarator cases (values in parentheses are arbitrarily chosen).

Case	M	aspect ratio	α^{Max} (radians)	θ_0^{Max} (radians)	$k_\theta^{Max}(\theta=0)\rho_i$
LHD	10	5.84	0.0	0.0	0.25
NCSX	3	4.47	0.0	0.0	0.65
NCSX-J=0	3	4.37	0.0	0.0	0.775
W7-X	5	10.45	0.39	0.0	(1.00)
HSX	4	10.0	0.1	0.0	0.65
QPS	2	2.66	0.35	0.0	0.65
NCSX-SYM	(1)	4.0	(0.0)	0.0	0.55

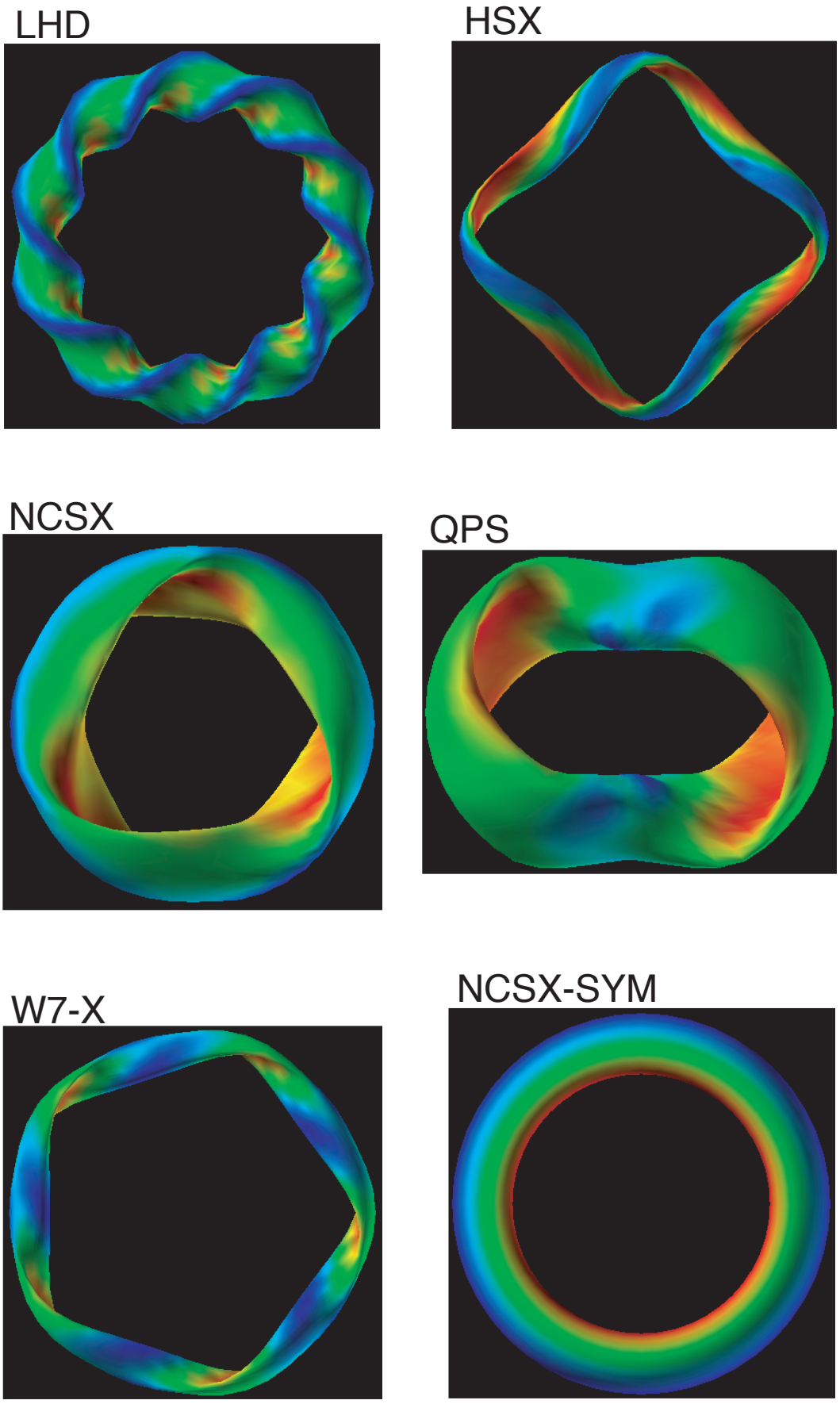

Fig. 1

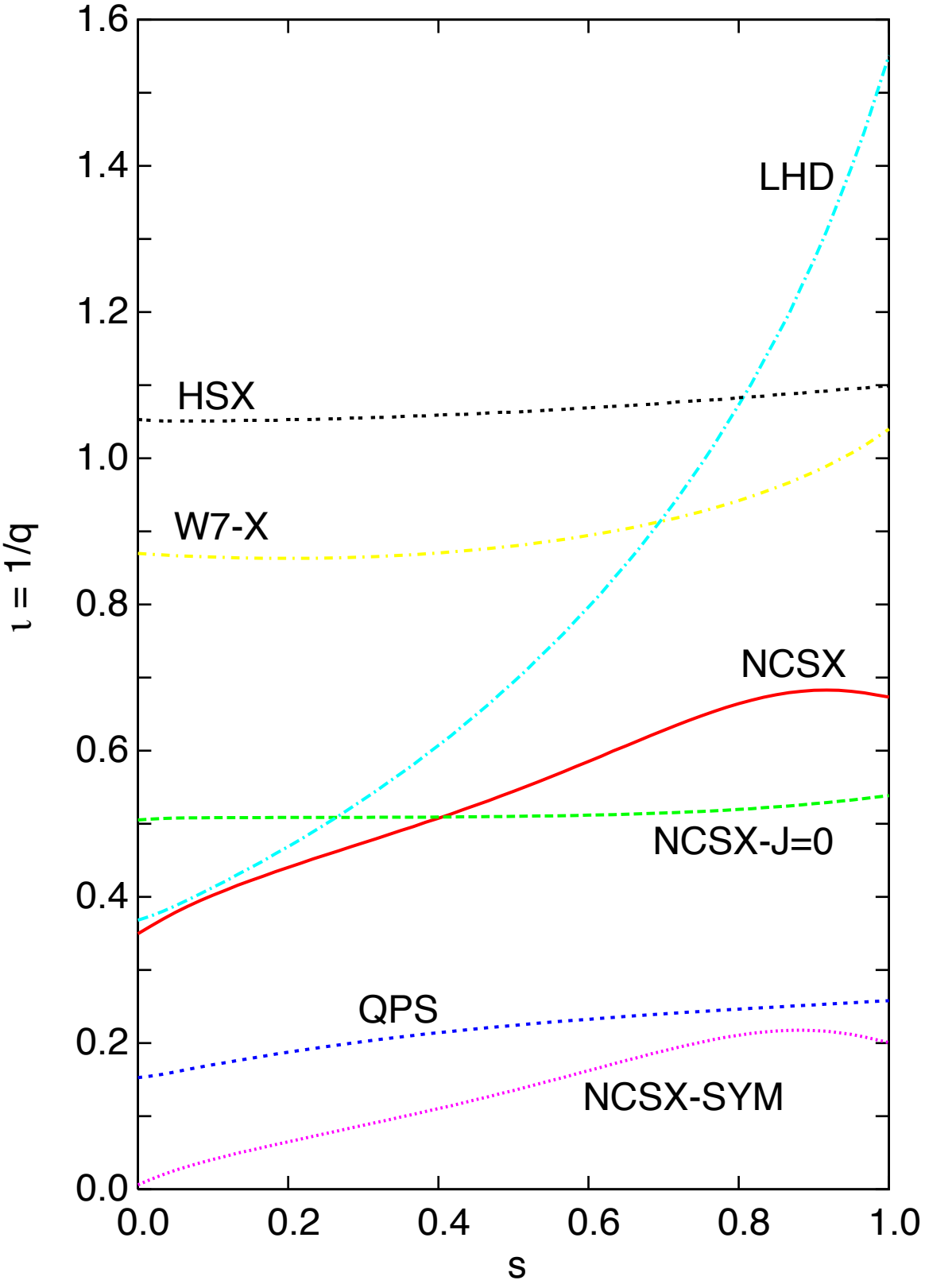
1.6
1.4
1.2
1.0
0.8
0.6
0.4
0.2
0.0
ι = 1/q
0.0
0.2
0.4
0.6
0.8
1.0
s
LHD
HSX
W7-X
NCSX
NCSX-J=0
QPS
NCSX-SYM

Fig. 2

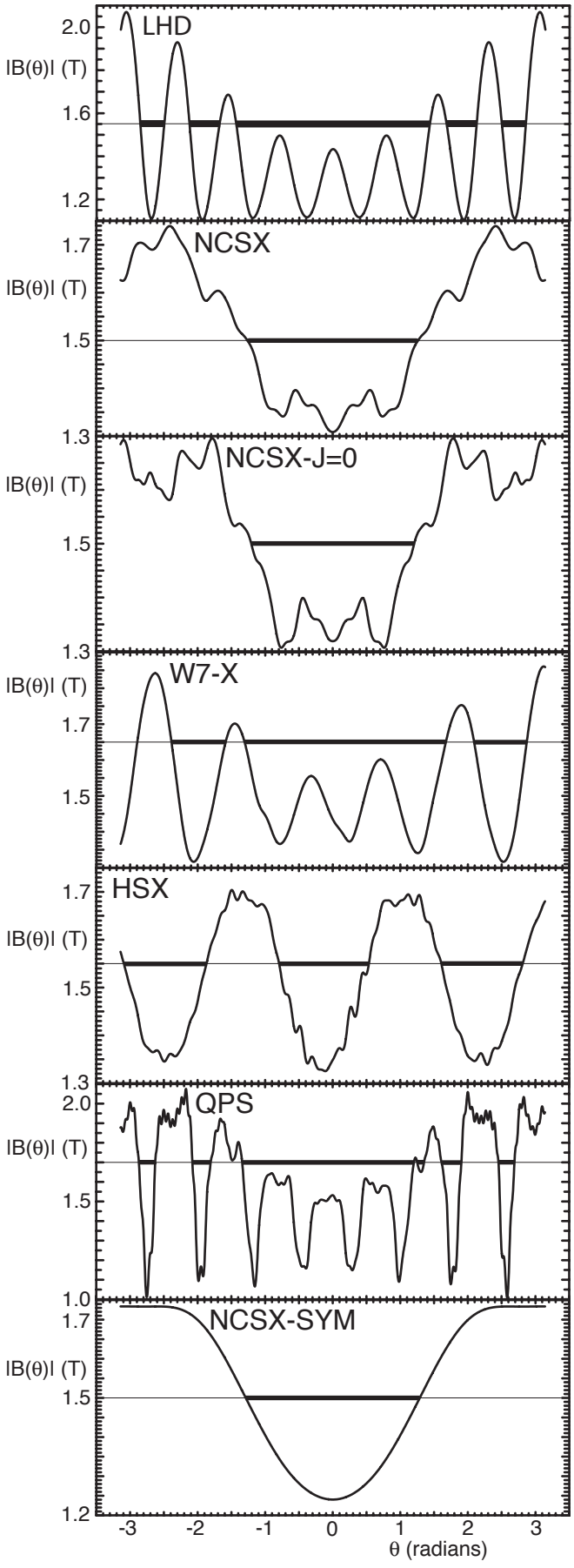

Fig. 3

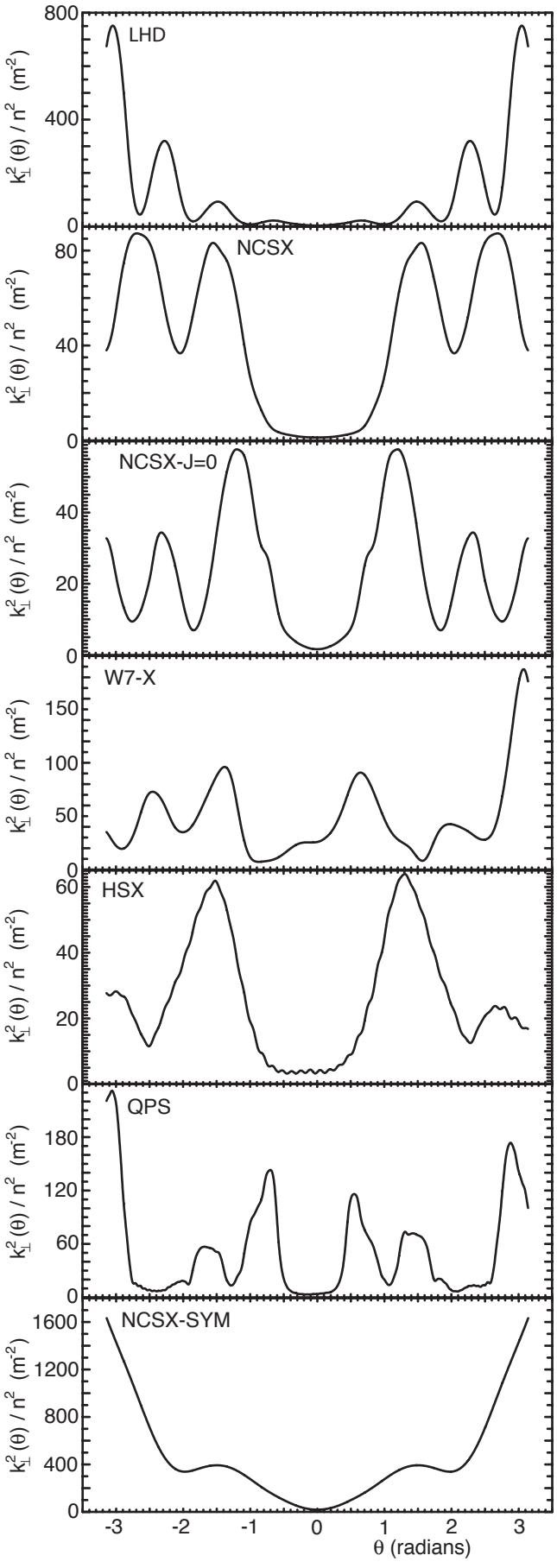
LHD
NCSX
NCSX-J=0
W7-X
HSX
QPS
NCSX-SYM
$k_\perp^2(\theta) / n^2$ (m^2)
θ (radians)

Fig. 4

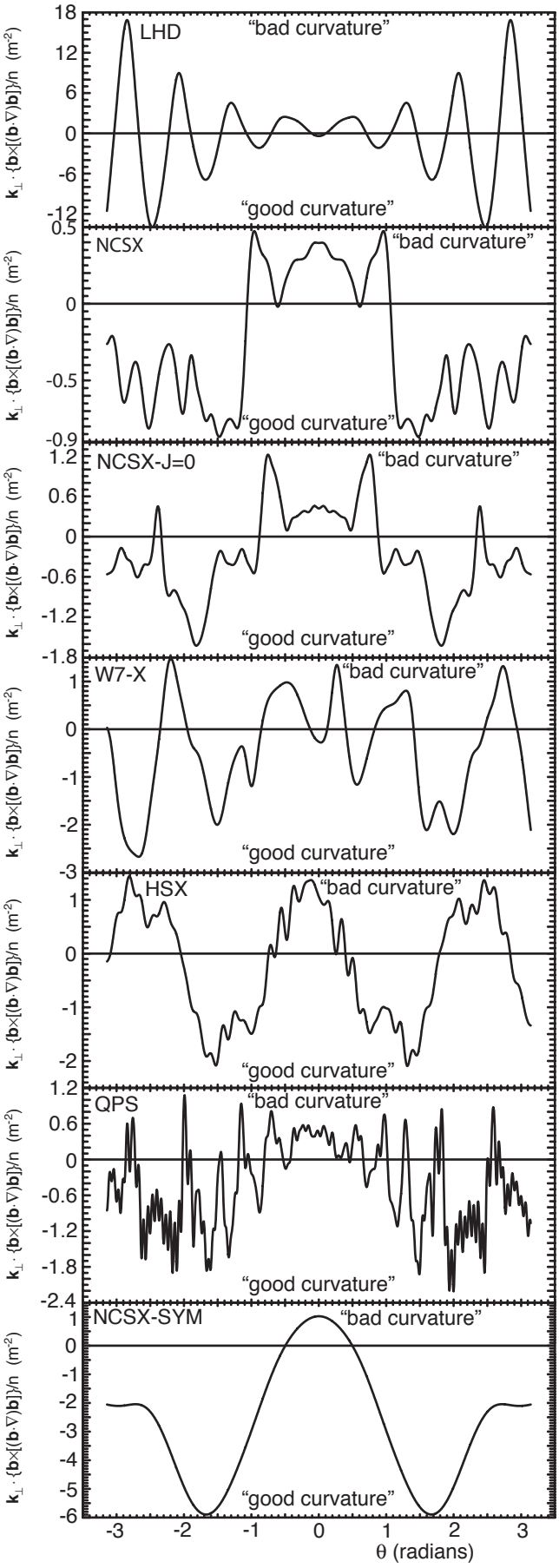
LHD
"bad curvature"
"good curvature"
NCSX
"bad curvature"
"good curvature"
NCSX-J=0
"bad curvature"
"good curvature"
W7-X
"bad curvature"
"good curvature"
HSX
"bad curvature"
"good curvature"
QPS
"bad curvature"
"good curvature"
NCSX-SYM
"bad curvature"
"good curvature"
$\mathbf{k}_\perp \cdot \{\mathbf{b}\times[(\mathbf{b}\cdot\nabla)\mathbf{b}]\}/n$ (m^{-2})
θ (radians)

Fig. 5

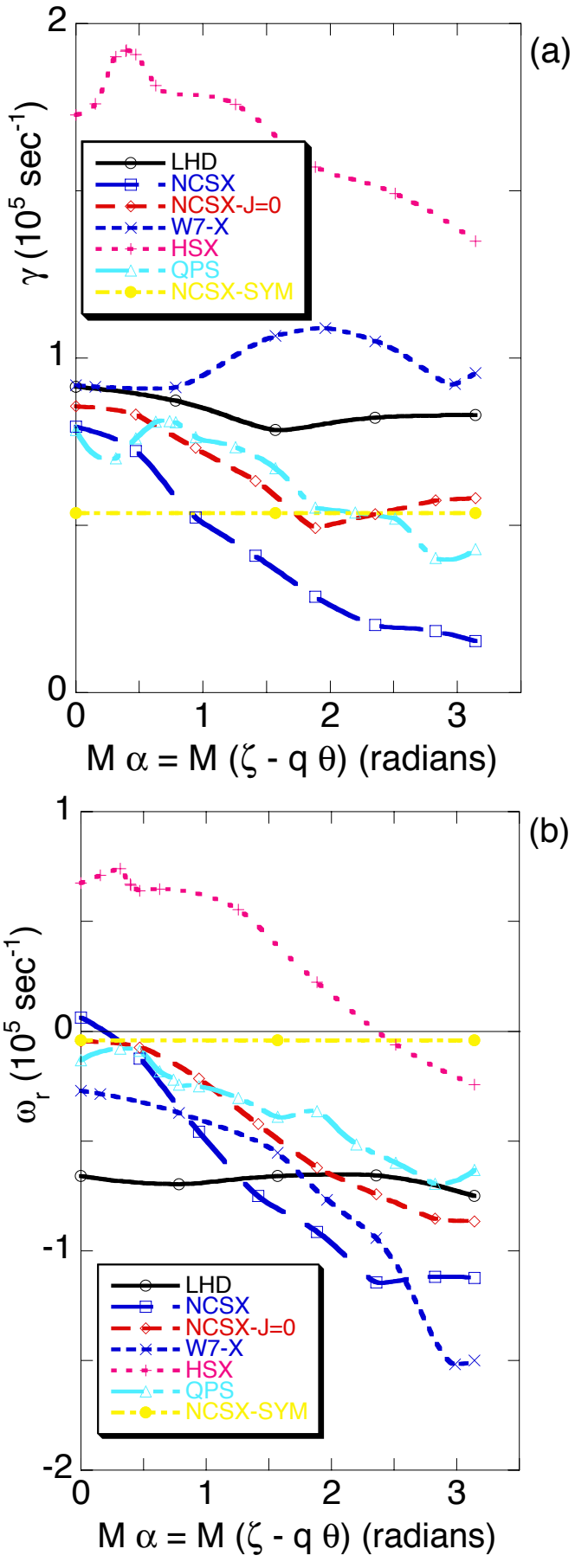
(a)
γ (10^5 sec^-1)
LHD
NCSX
NCSX-J=0
W7-X
HSX
QPS
NCSX-SYM
M α = M (ζ - q θ) (radians)
(b)
ω_r (10^5 sec^-1)
LHD
NCSX
NCSX-J=0
W7-X
HSX
QPS
NCSX-SYM
M α = M (ζ - q θ) (radians)

Fig. 6

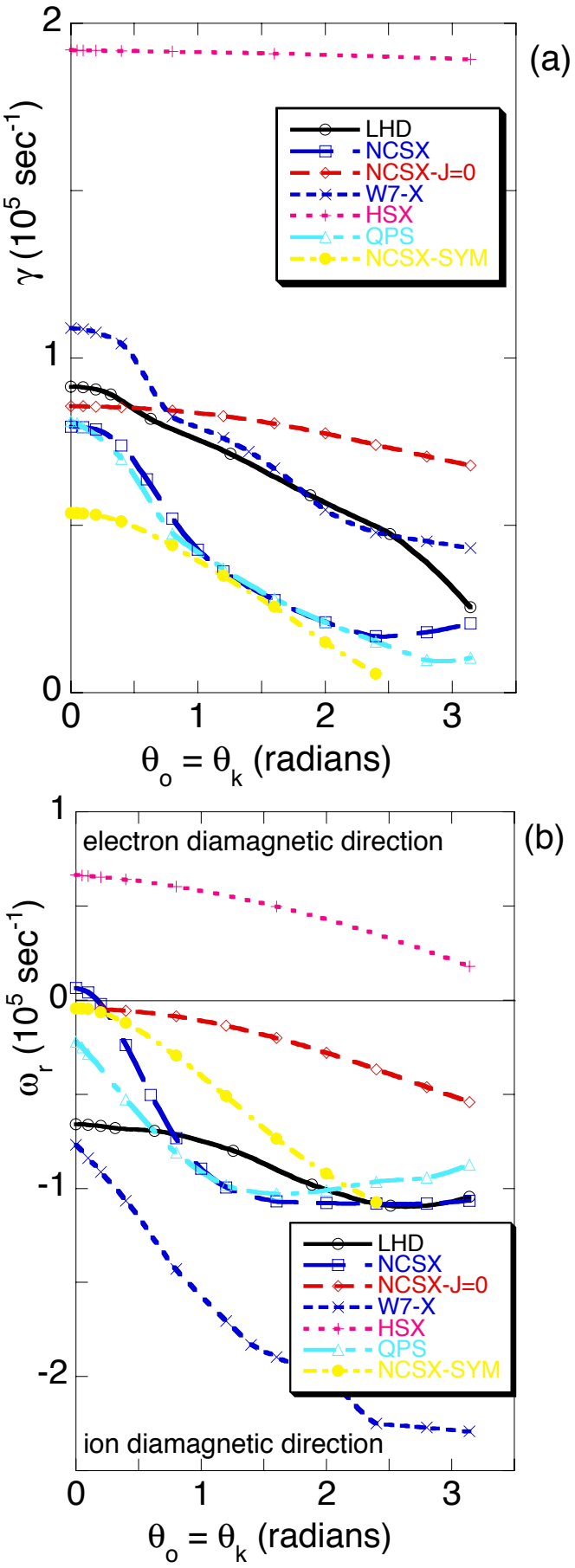
(a)
γ (10^5 sec^-1)
LHD
NCSX
NCSX-J=0
W7-X
HSX
QPS
NCSX-SYM
θ_o = θ_k (radians)
(b)
electron diamagnetic direction
ω_r (10^5 sec^-1)
ion diamagnetic direction
θ_o = θ_k (radians)

Fig. 7

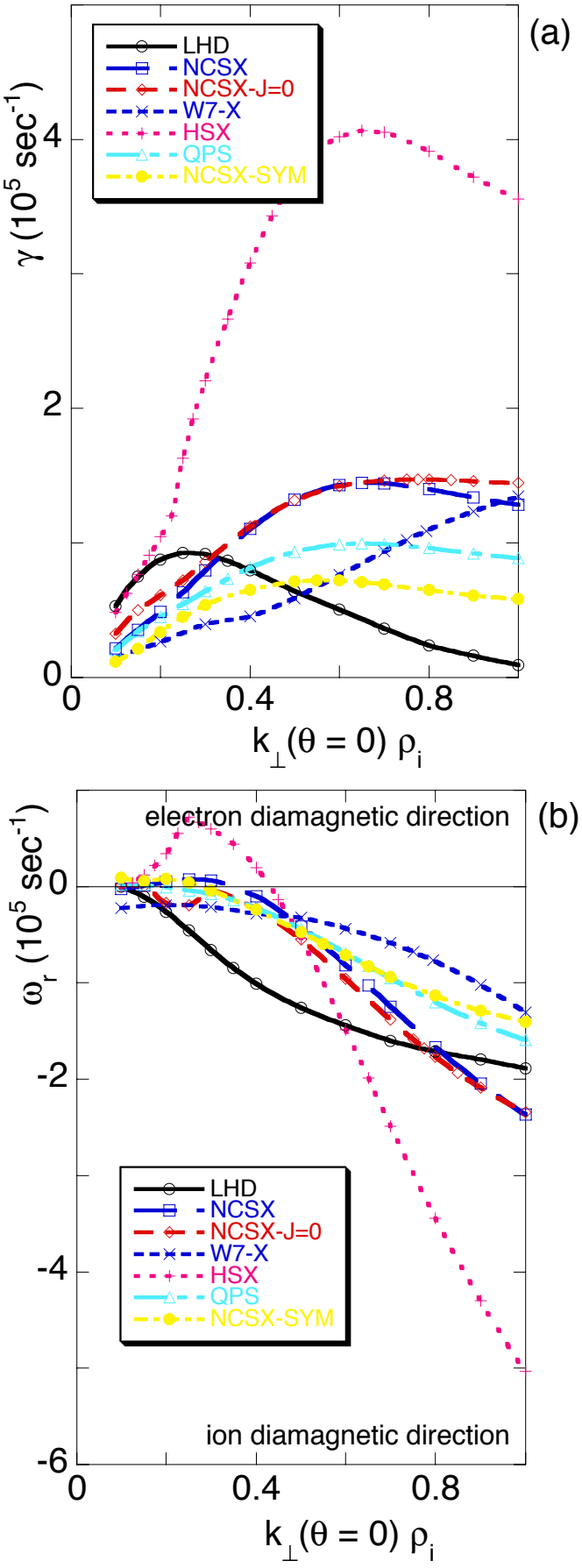
(a)
LHD
NCSX
NCSX-J=0
W7-X
HSX
QPS
NCSX-SYM
γ (10^5 sec^-1)
0
2
4
0
0.4
0.8
k⊥(θ = 0) ρi
(b)
electron diamagnetic direction
ion diamagnetic direction
ωr (10^5 sec^-1)
0
-2
-4
-6
0
0.4
0.8
k⊥(θ = 0) ρi

Fig. 8

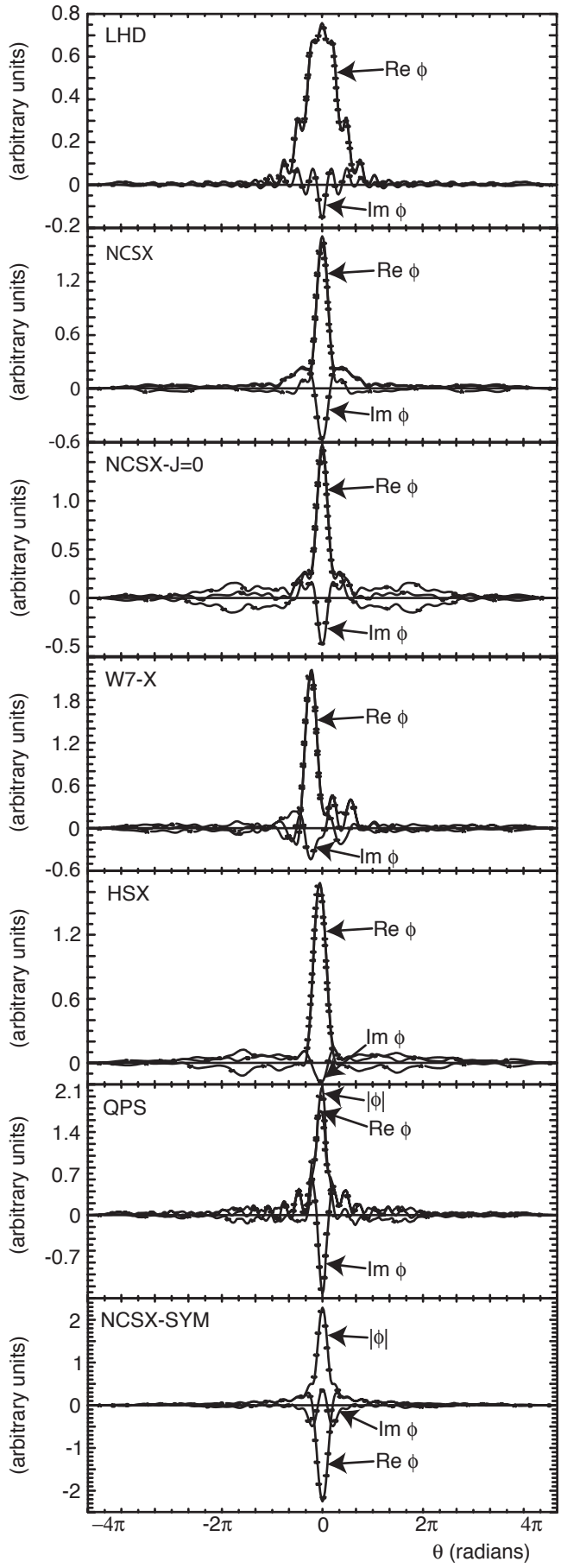
LHD
Re ϕ
Im ϕ
NCSX
Re ϕ
Im ϕ
NCSX-J=0
Re ϕ
Im ϕ
W7-X
Re ϕ
Im ϕ
HSX
Re ϕ
Im ϕ
QPS
|ϕ|
Re ϕ
Im ϕ
NCSX-SYM
|ϕ|
Im ϕ
Re ϕ
(arbitrary units)
θ (radians)
−4π
-2π
0
2π
4π

Fig. 9

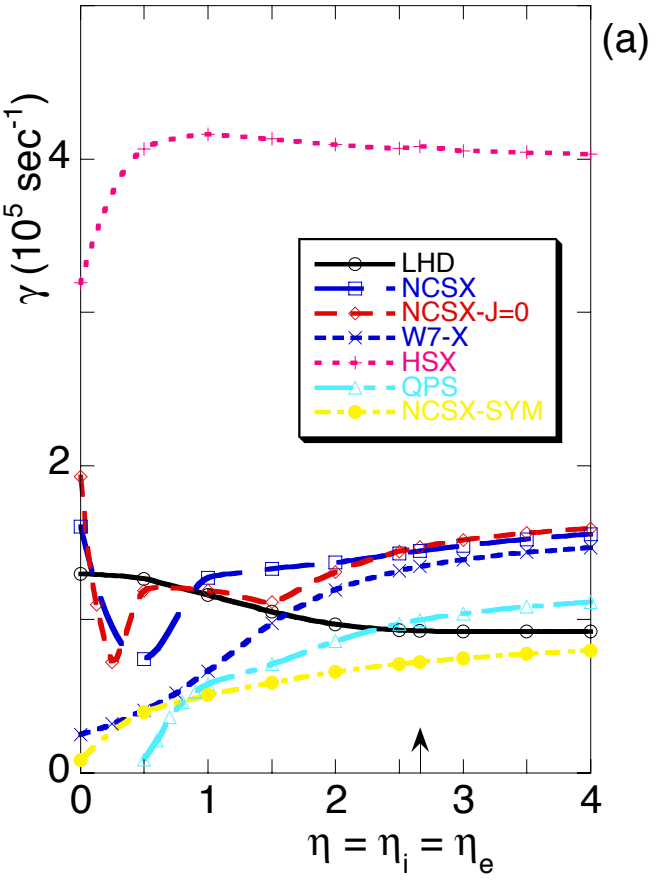
(a)
γ (10^5 sec^-1)
LHD
NCSX
NCSX-J=0
W7-X
HSX
QPS
NCSX-SYM
η = η_i = η_e

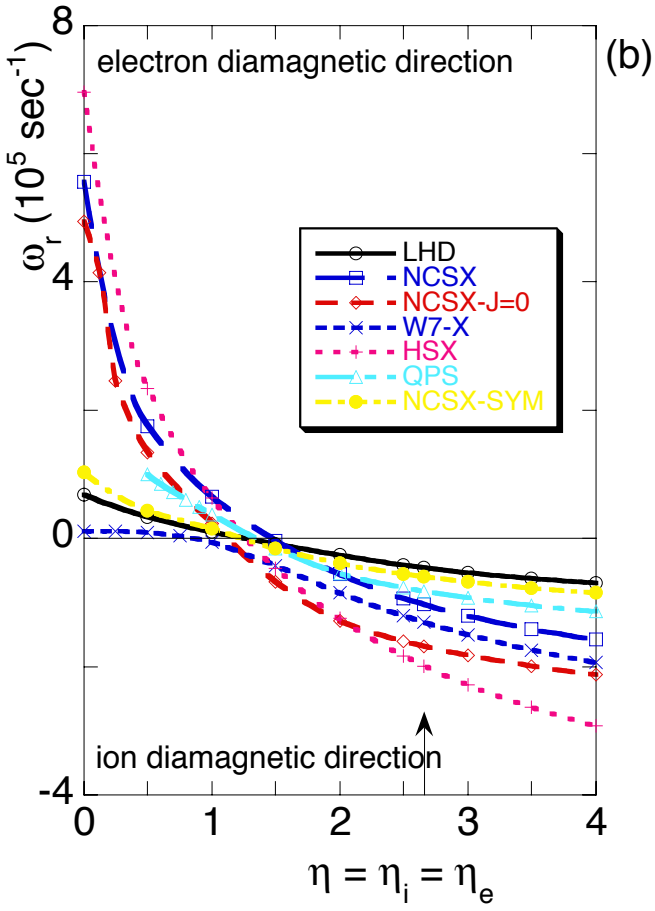
(b)
electron diamagnetic direction
ω_r (10^5 sec^-1)
LHD
NCSX
NCSX-J=0
W7-X
HSX
QPS
NCSX-SYM
ion diamagnetic direction
η = η_i = η_e

Fig. 10